

First-in-Human Assessment of the Novel PDE2A PET Radiotracer ^{18}F -PF-05270430

Mika Naganawa*¹, Rikki N. Waterhouse*², Nabeel Nabulsi¹, Shu-Fei Lin¹, David Labaree¹, Jim Ropchan¹, Sanela Tarabar², Nicholas DeMartinis², Adam Ogden², Anindita Banerjee², Yiyun Huang¹, and Richard E. Carson¹

¹Department of Radiology and Biomedical Imaging, PET Center, Yale School of Medicine, New Haven, Connecticut; and

²Pfizer Worldwide Research and Development, Cambridge, Massachusetts

This was a first-in-human study of the novel phosphodiesterase-2A (PDE2A) PET ligand ^{18}F -PF-05270430. The primary goals were to determine the appropriate tracer kinetic model to quantify brain uptake and to examine the within-subject test–retest variability. **Methods:** In advance of human studies, radiation dosimetry was determined in nonhuman primates. Six healthy male subjects participated in a test–retest protocol with dynamic scans and metabolite-corrected input functions. Nine brain regions of interest were studied, including the striatum, white matter, neocortical regions, and cerebellum. Multiple modeling methods were applied to calculate volume of distribution (V_T) and binding potentials relative to the nondisplaceable tracer in tissue (BP_{ND}), concentration of tracer in plasma (BP_P), and free tracer in tissue (BP_f). The cerebellum was selected as a reference region to calculate binding potentials. **Results:** The dosimetry study provided an effective dose of less than 0.30 mSv/MBq, with the gallbladder as the critical organ; the human target dose was 185 MBq. There were no adverse events or clinically detectable pharmacologic effects reported. Tracer uptake was highest in the striatum, followed by neocortical regions and white matter, and lowest in the cerebellum. Regional time–activity curves were well fit by multilinear analysis-1, and a 70-min scan duration was sufficient to quantify V_T and the binding potentials. BP_{ND} , with mean values ranging from 0.3 to 0.8, showed the best intrasubject and intersubject variability and reliability. Test–retest variability in the whole brain (excluding the cerebellum) of V_T , BP_{ND} , and BP_P were 8%, 16%, and 17%, respectively. **Conclusion:** ^{18}F -PF-05270430 shows promise as a PDE2A PET ligand, albeit with low binding potential values.

Key Words: phosphodiesterase 2A; positron emission tomography; test–retest reproducibility; dosimetry; brain imaging

J Nucl Med 2016; 57:1388–1395

DOI: 10.2967/jnumed.115.166850

Phosphodiesterase enzymes (PDEs) hydrolyze cyclic adenosine monophosphate (cAMP) and cyclic guanosine monophosphate (cGMP) into their corresponding monophosphates. By this hydrolysis, the signals generated by these molecules are terminated. The phosphodiesterase gene superfamily consists of 11 gene families that

express PDEs (1). PDE2 (phosphodiesterase-2A), which possesses protein motifs (GAF domains) that regulate dimerization of the enzyme, and may also constitute an allosteric site that is activated by cGMP, is characterized by a high Michaelis constant K_m for both cGMP and cAMP ($>5 \mu\text{M}$) (2). Agents that stimulate cGMP production, such as nitric oxide synthase activators or natriuretic peptides, activate PDE2A and cause hydrolysis of cAMP.

In the central nervous system, PDE2A is highly expressed in the striatum, hippocampus, frontal cortex, olfactory neurons, and medial habenula (3) and plays a role in regulating neurotransmission. In non-central nervous system tissues, PDE2A is highly expressed in adrenal glands and vascular endothelial cells in which it may regulate vascular permeability (4). The development of a PDE2A radioligand would allow the evaluation of disease-specific changes (e.g., in schizophrenia) and potential inhibitor drugs.

We recently reported selection criteria for successful site-specific PET ligands, including PDE2A radiotracers (5). The companion paper reports that the PET ligand ^{18}F -PF-05270430 is a potent inhibitor with high binding affinity for PDE2A (6). It shows excellent selectivity over other PDE subtypes and has good properties for PET imaging, as evaluated in nonhuman primates.

In this study, we present nonhuman primate dosimetry results and first-in-human PET data. Along with evaluating the safety and tolerability of ^{18}F -PF-05270430 in healthy human participants, we evaluated appropriate analytic strategies for tracer binding to PDE2A sites and assessed subject test–retest variability.

MATERIALS AND METHODS

Radiotracer Synthesis

^{18}F -PF-05270430 was prepared as described in the companion paper (6) and in the supplemental materials (available at <http://jnm.snmjournals.org>). Radiochemical purity of the final product solution was greater than 98%. Specific activity at the end of synthesis was $115 \pm 53 \text{ GBq}/\mu\text{mol}$ ($n = 12$).

Monkey Dosimetry Studies

Four rhesus monkeys (2 male and 2 female; mean weight \pm SD, $8.95 \pm 3.42 \text{ kg}$) underwent whole-body dynamic PET scans on a Biograph mCT (Siemens Medical Systems) after intravenous injection of ^{18}F -PF-05270430. Animals were scanned for approximately 3 h in a sequence of 14–17 passes with either 4 or 5 bed positions from the top of the head to mid thigh. Scans were visually inspected for organ activity exceeding background level. Included organs were the liver, kidneys, urinary bladder, heart, spleen, gallbladder, brain, red marrow (femur), upper large intestines, small intestines, stomach wall, pancreas, ovaries, and cortical bone. Using early and later summed images, we delineated manually regions of interest (ROIs), and mean organ activity values were computed to form time–activity curves.

Received Dec. 22, 2015; revision accepted Mar. 14, 2016.

For correspondence contact: Mika Naganawa, Department of Radiology and Biomedical Imaging, PET Center, Yale School of Medicine, P.O. Box 208048, New Haven, CT 06520.

E-mail: mika.naganawa@yale.edu

*Contributed equally to this work.

Published online Apr. 21, 2016.

COPYRIGHT © 2016 by the Society of Nuclear Medicine and Molecular Imaging, Inc.

Decay correction was removed to reflect actual activity in each organ, and integrated activity ($\text{Bq}\cdot\text{h}/\text{cm}^3$) was computed using isotope decay to extrapolate to infinity after the scan period. These values were multiplied by the organ volumes of a standard 70-kg (male) and 55-kg (female) reference mathematic phantom (7), scaled by animal mass/body weight and then normalized to injected activity to obtain organ residence times (N , hour), which were entered into the OLINDA software (8) to obtain absorbed doses in all organs. Doses to the stomach were adjusted to reflect the presence of activity in the stomach wall rather than the contents.

Human Subjects

Healthy male volunteers (age, 24–54 y; weight, 87.5 ± 14.1 kg) with no clinically significant diseases completed a test–retest study. The institutional review board–approved study was also approved by the Yale–New Haven Hospital Radiation Safety Committee and performed in accordance with federal guidelines and regulations of the United States for the protection of human research subjects contained in Title 45 part 46 of the Code of Federal Regulations. All subjects signed a written informed consent form.

Human Brain PET Studies

PET Imaging. Each subject underwent 2 PET scans with ^{18}F -PF-05270430. In advance of each scan, an intravenous line was placed for tracer injection, and an arterial line was placed for measurement of the input function. The test and retest scans were 4.7 ± 0.8 d apart. Each subject was limited to a maximum dose of 185 MBq per scan, based on dosimetry study results. The mass dose in clinical PET studies was limited to 10 μg or less per administration. The choice of dose was based on rat safety toxicity studies, which showed that doses were well tolerated up to the maximum dose tested (3 $\mu\text{g}/\text{kg}$). In the clinic, safety was assessed by measurement of vital signs (blood pressure, heart rate, oxygen saturation, and hematocrit) and recording of adverse symptoms after tracer administration.

^{18}F -PF-05270430 was administered intravenously over 1 min by an automatic pump (Harvard PHD 22/2000; Harvard Apparatus). PET scans were then obtained with an ECAT EXACT HR+ scanner (Siemens Medical Systems) in 3-dimensional mode. For the first 3 subjects, the acquisition duration was 240 min, consisting of a 120-min scan, 30-min break, and a 90-min scan. The scan duration was shortened to 120 min for subjects 4–6 based on analysis of the initial data. Dynamic scan data were reconstructed with corrections for attenuation (transmission scan), normalization, scatter, randoms, and dead time using the ordered subset–expectation maximization algorithm (4 iterations, 16 subsets) in 33 frames (6×0.5 , 3×1 , 2×2 , and 22×5 min) for the 120-min scan plus 18 frames (18×5 min) for the scan from 150 to 240 min.

MRI. Before the PET scans, each subject underwent an MR scan for PET image registration. MR imaging was performed using a 3-dimensional magnetization-prepared rapid gradient-echo pulse sequence with an echo time of 2.78 ms, repetition time of 2,500 ms, inversion time of 1,100 ms, and flip angle of 7° on a 3-T whole-body scanner (Trio; Siemens Medical Systems) with a circularly polarized head coil.

Arterial Input Function Measurement. Continuous and discrete blood samples were taken for determination of whole-blood activity and the metabolite-corrected plasma input function. For the first 7 min, arterial blood was continuously counted using an automated blood counter (PBS-101; Veenstra Instruments). Discrete blood samples were manually collected at 3, 5, 8, 10, 15, 20, 25, 30, 40, 50, 60, 75, 90, 105, and 120 min after dosing. Additional samples were obtained at 150, 180, 210, and 240 min for the 240-min scan.

Plasma analysis of radiotracer metabolism was performed from samples collected at 5, 15, 30, 60, 90, and 120 min after injection (plus 180 and 240 min for the 240-min scans). Metabolite analysis

was performed using the column-switching high-performance liquid chromatography (HPLC) method (9) to determine the parent fraction. An ultrafiltration-based method (Centrifree; Millipore) was used for measuring the plasma free fraction (f_p). Details are provided in the supplemental materials.

At the retest scan of 1 subject, no arterial line was available. This subject was excluded from calculation of test–retest variability. For another subject, the f_p value of the test scan was excluded from calculation of mean and SD of f_p because of contaminated samples.

Image Registration and ROIs. For each subject, motion correction of each dynamic frame was performed by registration to a summed PET image (0–10 min after injection) using a 6-parameter mutual information algorithm (FMRIB's Linear Image Registration Tool [FLIRT], FSL). The summed PET image was then coregistered to the subject's T1-weighted MR image (6-parameter affine registration), which was subsequently coregistered to the automated anatomic labeling template (10) in Montreal Neurologic Institute (11) space using a nonlinear transformation (Bioimage Suite; Yale University) (12). Regional time–activity curves were generated for the putamen, caudate, nucleus accumbens, temporal cortex, occipital cortex, parietal cortex, frontal cortex, cerebellum, and centrum semiovale using the combined transformations from template-to-PET space.

Quantitative Analysis. Regional distribution volumes (V_T) and binding potentials relative to the nondisplaceable tracer in tissue (BP_{ND}), concentration of tracer in plasma (BP_P), and free tracer in tissue (BP_F) were computed using 1-tissue (1TC) and 2-tissue (2TC)-compartment models, and multilinear analysis-1 (MA1) with the plasma input function. The simplified reference tissue model (SRTM) was also used to derive BP_{ND} directly. Blood volume in the brain was assumed to be 5% in all models. The equation for MA1 with blood volume correction (13) was:

$$C_{PET}(t) = -\frac{V_T}{b} \int_0^t C_P(u) du + \frac{1}{b} \int_0^t C_{PET}(u) du - \frac{F_V}{b} \int_0^t C_{WB}(u) du + F_V C_{WB}(t),$$

where $C_{PET}(t)$, $C_P(t)$, and $C_{WB}(t)$ represent the tissue, plasma, and whole-blood time–activity curves, respectively, and F_V is the fractional blood volume. To calculate binding potentials, the cerebellum was used as a reference region because no PDE2A signal was detected in the cerebellum in an in vitro immunoreactivity study of human brain extracts with an anti-PDE2A antibody (4). For parameter estimation, data points were weighted on the basis of noise equivalent counts. Percentage SE (%SE; [SE]/[estimated parameter]) was estimated from the theoretic covariance matrix.

Effect of Scan Time. The time stability of V_T estimates was evaluated by fitting the MA1 model ($t^* = 40$ min) to time–activity curves with shortened scan durations ranging from 50 to 120 min ($n = 11$). The ratio, r , of V_T values from the shortened scan to those from the 120-min scan was computed for each ROI and duration. The minimum acceptable scan duration was the one that satisfied the following 2 criteria (14): the mean ratio (r) across subjects was between 0.95 and 1.05, and the interindividual SD of the ratio (r) was less than 0.1. We also compared 120-min V_T estimates with those from longer scans (160–240 min; $n = 6$: 3 subjects \times 2 scans each).

Statistical Analyses. The reproducibility of the outcome measures was assessed with test–retest variability (TRV) and absolute TRV (aTRV). TRV was calculated as:

$$\text{TRV} = \frac{p(T) - p(R)}{(p(T) + p(R))/2}$$

where $p(T)$ and $p(R)$ are parameter estimates at test and retest conditions, respectively. The mean of TRV indicates the presence

TABLE 1
Subject Information and PET Scan Parameters

Parameter	Humans		Monkeys, dosimetry ($n = 4$)
	Test ($n = 6$)	Retest ($n = 6$)	
Injected dose (MBq)	182 ± 3	174 ± 9	135 ± 71
Specific activity at time of injection (MBq/nmol)	83.9 ± 51.4	83.6 ± 32.4	72.9 ± 46.9
Injected mass (µg/kg)	0.024 ± 0.032	0.013 ± 0.010	0.11 ± 0.09

Data are mean ± SD. Age was 37 ± 12 and 8 ± 2 y for humans and monkeys, respectively. Body weight was 87.5 ± 14.1 and 9.0 ± 3.4 kg for humans and monkeys, respectively.

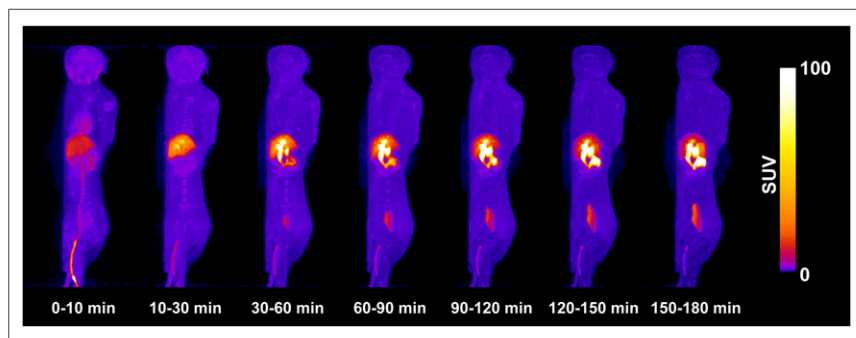


FIGURE 1. Maximum-intensity projection (coronal view) over 3 h of ^{18}F -PF-05270430 in male rhesus monkey.

of a trend between the 2 scans, and the SD of TRV is an index of the variability of the percentage difference between 2 measurements. aTRV uses absolute values of TRV, and its mean indicates the coefficient of variation when the mean of TRV was 0 (15). Reliability was also assessed by the intraclass correlation coefficient (ICC), ranging from -1 (no reliability) to +1 (maximum reliability).

TABLE 2
Organ Residence Times

Organ	N (h)
Marrow	0.032 ± 0.007
Brain	0.033 ± 0.013
Gallbladder	0.095 ± 0.031
Heart	0.009 ± 0.002
Intestine	0.107 ± 0.052
Kidneys	0.069 ± 0.030
Liver	1.147 ± 0.306
Lungs	0.025 ± 0.005
Stomach	0.008 ± 0.006
Urinary bladder	0.063 ± 0.040
Total	1.588 ± 0.306

Values are mean ± SEM ($n = 4$).

RESULTS

Nonhuman Primate Dosimetry Study

Scan parameters for these experiments are summarized in Table 1. Figure 1 shows an example of the whole-body distribution over time. The main route of elimination was hepatobiliary, with the gallbladder having the highest radioactivity uptake. Organ residence times are listed in Table 2, and accounted for 61% ± 23% of the theoretic value. Table 3 shows absorbed doses derived from the male and female phantoms ($n = 4$). Under CFR 361.1 (for single study, 50 mSv per organ or 30 mSv to selected organs undergoing rapid cell division, whichever is less), the gallbladder is

the dose-limiting organ with a single-study dose limit of 306 and 249 MBq for the male and female phantoms, respectively. The dose to the liver was slightly less than that of the gallbladder. On the basis of these values, a target dose of 185 MBq (5 mCi) was chosen for human studies.

Human Injection and Scan Parameters

The mean administered activity was 178 ± 8 MBq (range, 157–185 MBq). Injection and scan parameters are listed in Table 1. The injected dose and injected mass did not significantly differ between test and retest scans (paired t test, $P > 0.05$). We detected no relationship between BP_{ND} and injected mass, suggesting that we were working in the tracer range, because a negative correlation was not found.

Safety

There were no adverse events or clinically detectable pharmacologic effects reported in any of the 6 subjects. No significant changes in vital signs were observed. Each subject completed both scans without reporting discomfort that would warrant cessation of scanning.

Plasma Analysis

Plasma data for the test and retest scans are displayed in Figures 2A–2C. The fraction of ^{18}F -PF-05270430 plasma radioactivity decreased moderately over time, from 93% ± 3% at 5 min to 40% ± 4% at 120 min ($n = 11$). A typical example of a high-performance liquid chromatogram (90 min after injection) is shown in Figure 2D. The retention time was 11–12 min, and the HPLC profile revealed metabolites that were less lipophilic than

TABLE 3
Radiation Absorbed Dose for ^{18}F -PF-05270430

Organ	70-kg man		55-kg woman	
	Mean (mSv/MBq)	SD (mSv/MBq)	Mean (mSv/MBq)	SD (mSv/MBq)
Adrenals	1.55E-02	6.41E-03	1.84E-02	7.19E-03
Brain	4.76E-03	3.18E-03	6.80E-03	4.57E-03
Breasts	3.01E-03	1.43E-03	3.51E-03	1.65E-03
Gallbladder wall	1.63E-01	8.79E-02	2.01E-01	1.08E-01
Lower large intestine wall	6.61E-02	6.27E-02	7.01E-02	6.58E-02
Small intestine	7.32E-03	2.67E-03	9.04E-03	3.29E-03
Stomach wall	9.56E-03	6.66E-03	1.18E-02	7.80E-03
Upper large intestine wall	8.97E-03	3.42E-03	1.10E-02	4.14E-03
Heart wall	9.83E-03	4.17E-03	1.22E-02	5.24E-03
Kidneys	5.11E-02	3.20E-02	5.81E-02	3.65E-02
Liver	1.49E-01	8.02E-02	1.84E-01	9.91E-02
Lungs	1.13E-02	4.53E-03	1.36E-02	5.34E-03
Muscle	3.67E-03	1.38E-03	4.46E-03	1.65E-03
Ovaries			8.32E-03	4.51E-03
Pancreas	1.40E-02	5.95E-03	1.70E-02	7.12E-03
Red marrow	6.89E-03	2.44E-03	7.20E-03	2.47E-03
Osteogenic cells	4.19E-03	1.55E-03	5.48E-03	2.00E-03
Skin	1.87E-03	7.46E-04	2.24E-03	8.82E-04
Spleen	5.76E-03	3.62E-03	7.36E-03	4.01E-03
Testes	1.26E-03	6.91E-04		
Thymus	2.61E-03	1.16E-03	3.18E-03	1.41E-03
Thyroid	7.12E-04	2.83E-04	8.57E-04	3.57E-04
Urinary bladder wall	3.22E-02	3.76E-02	4.34E-02	5.11E-02
Uterus			6.24E-03	2.83E-03
Total body	7.93E-03	3.26E-03	9.56E-03	3.85E-03
Effective dose equivalent	3.22E-02	1.07E-02	3.88E-02	1.29E-02
Effective dose	2.28E-02	8.21E-03	2.69E-02	9.28E-03

parent tracer. The f_p was 0.13 ± 0.03 ($n = 10$). There was no statistically significant difference in f_p between test and retest scans (2-sided unpaired t test, $P = 0.76$). The TRV of f_p was $-4\% \pm 30\%$ ($n = 4$).

Brain Distribution and Kinetics

Figure 3 shows typical SUV images of ^{18}F -PF-05270430. The highest uptake was seen in the putamen, caudate, and nucleus accumbens, followed by cortical regions and cerebellum. This was expected based on the known relative distribution of PDE2A in the central nervous system and on the nonhuman primate PET imaging studies performed in the companion paper (6). The radioactivity cleared from all ROIs relatively quickly, resulting in SUVs of less than 1 by 30 min after injection. In later frames, uptake in white matter was more pronounced than in gray matter (Fig. 3B) because of slower kinetics (Supplemental Fig. 1).

Typical time–activity curves and fitted curves are shown in Figure 4. Time–activity curves were fitted well with a 2TC model. 2TC K_1 estimates ($\text{mL}/\text{min}/\text{cm}^3$) ranged from 0.041 ± 0.004 (centrum semiovale) to 0.112 ± 0.010 (putamen). 2TC V_T estimates without blood volume correction were similar to those with correction (V_T [uncorrected] = $1.01 \times V_T$ [corrected] + 0.03 , $R^2 = 1.00$), whereas 2TC BP_{ND} estimates without blood volume

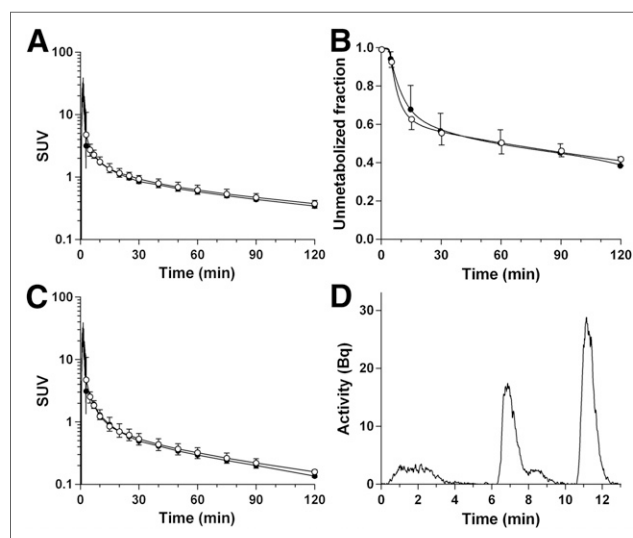


FIGURE 2. Mean \pm SD of total plasma activity (A), plasma parent fraction (B), and metabolite-corrected plasma activity (C) in the test (\bullet , $n = 6$) and retest (\circ , $n = 5$) scans. (D) HPLC plasma analysis at 90 min after injection. A and C are displayed in SUV units (concentration/[injected dose/body weight]).

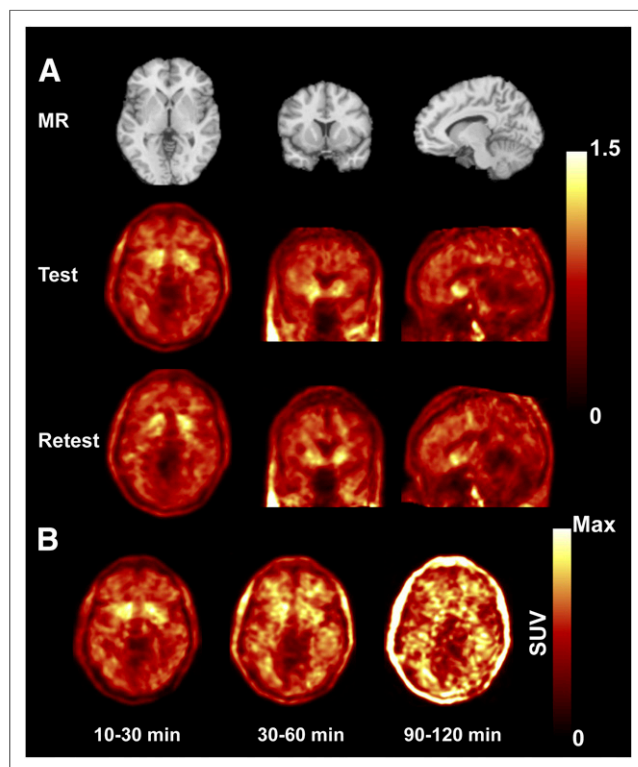


FIGURE 3. (A) MR and coregistered typical PET images in test and retest conditions (10–60 min after injection of ^{18}F -PF-05270430). PET images are displayed in SUV units. (B) PET images showing temporal distribution over 2 h, with each image scaled to its own maximum (SUV_{max} scales were 2, 1, and 0.4 for 10–30, 30–60, and 90–120 min, respectively). Max = maximum.

correction were slightly lower than corrected values (BP_{ND} [uncorrected] = $0.96 \times BP_{\text{ND}}$ [corrected] - 0.00, $R^2 = 1.00$). MA1 ($t^* = 40$ min) and SRTM fits were also excellent, whereas a moderate lack of fit was seen with a 1TC model. Although 2TC fits

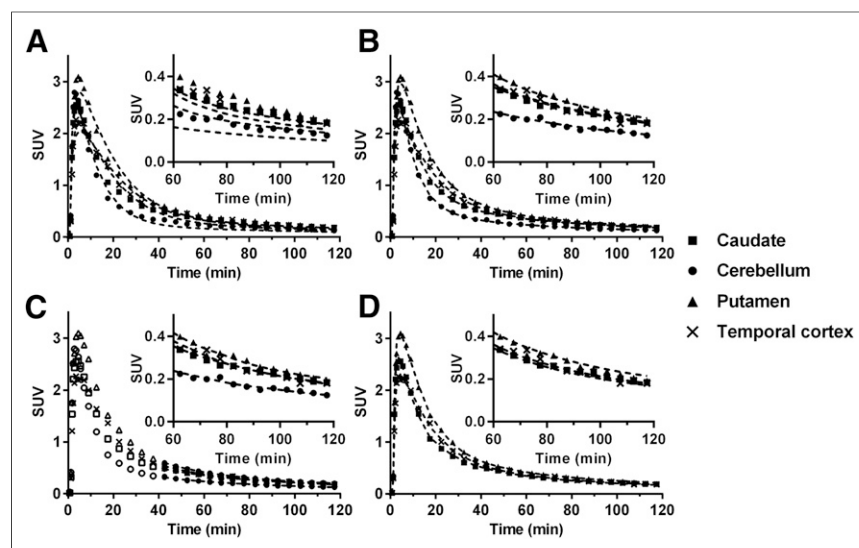


FIGURE 4. Time-activity curves from putamen, temporal cortex, caudate, and cerebellum of ^{18}F -PF-05270430. Fits with 1TC (A), 2TC (B), MA1 ($t^* = 40$ min) (C), and SRTM (D) are displayed as dotted lines. Insets show last 60 min.

were excellent, 2TC parameters could not be reliably estimated in some cases ($\%SE > 25\%$ in 6/99 fits). After estimates with large $\%SE$ were excluded, there was excellent correlation between 2TC and MA1 for V_T and BP_{ND} (Fig. 5). SRTM BP_{ND} values were well correlated with the 2TC values but with a slope and intercept offset from the line of identity (Fig. 5B). The multi-linear reference tissue model was also applied, but it produced many unstable BP_{ND} estimates in high-binding regions with all t^* settings that were tested (data not shown).

Given the quality of fit and comparison with 2TC estimates, the model of choice is MA1 ($t^* = 40$ min), when arterial data are available. MA1 V_T estimates using different t^* values had small differences from the 40-min values, ranging from $-2.1\% \pm 1.5\%$ ($t^* = 10$ min) to $+1.0\% \pm 0.6\%$ ($t^* = 60$ min). Mean distribution volumes and binding potentials are shown in Table 4. V_T was highest in the putamen and caudate, followed by neo-cortical regions and white matter, and lowest in the cerebellum. Intersubject variability was 7%–14% for V_T , 9%–24% for BP_{ND} , and 8%–23% for BP_P ($n = 5$) and 7%–15% for V_T/f_P and 6%–33% for BP_F ($n = 4$).

The minimum scan duration required to satisfy stability criteria was 70 min for MA1 ($t^* = 40$ min) (Supplemental Fig. 2). With increasing scan duration, V_T estimates showed small increases ($<10\%$, Supplemental Table 1). For higher-binding regions, the change in V_T values (240 vs. 120 min) was small (1.0%–1.9%), with the largest change (9%) in the parietal cortex.

Test-Retest Variability and Reproducibility of Binding Parameters

Table 5 shows the test-retest statistics for V_T and binding potentials, which were similar across regions. V_T showed aTRV less than 10% in all regions, and the global mean of TRV was -4% . Both BP_{ND} and BP_P showed moderate aTRV ($\sim 15\%$), with a global mean TRV of 0% (BP_{ND}) and -5% (BP_P). For V_T , the ICC was good (>0.6) except in the putamen (0.23), and ICC tended to be lower for BP_{ND} except for the caudate, putamen, and frontal cortex. BP_{ND} using SRTM showed statistics similar to BP_{ND} using MA1. For BP_P , the ICC was poor in most regions (<0.6). Scaling with f_P (V_T/f_P , BP_F) led to poor reproducibility with an aTRV of approximately 20% (V_T/f_P) and approximately 25% (BP_F) and lower reliability.

DISCUSSION

The aims of this study were to determine the dosimetry of the novel PDE2A tracer ^{18}F -PF-05270430 and perform a first-in-human study. To our knowledge, ^{18}F -PF-05270430 is the first PDE2A radiotracer evaluated in humans. All subjects tolerated the tracer well without adverse effects. Modeling methods were evaluated, and regional brain test-retest variability was determined.

PDE2A is known to be involved in the pathophysiology of cognitive disorders (16) and other disease states. Thus, noninvasively imaging PDE2A enzymes could be used to facilitate the development

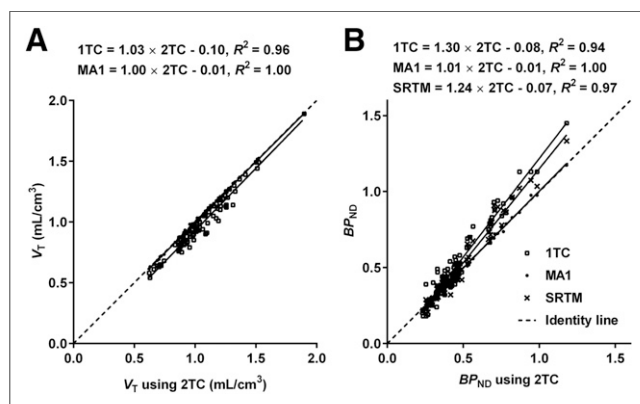


FIGURE 5. Comparison of 1TC and MA1 V_T estimates against 2TC V_T estimates (A) and 1TC, MA1, and SRTM BP_{ND} estimates against 2TC BP_{ND} estimates (B). Solid line = linear regression fit. All values were estimated with blood volume correction.

of PDE2A inhibitors. This technique enables the capability to quantitatively measure PDE2A enzyme occupancy levels of drugs, which is a prerequisite for expression of PDE2-mediated pharmacology and target modulation (17). In turn, this allows for understanding the relationship between drug concentrations and PDE2A enzyme occupancy. In addition, differences in PDE2A enzyme levels in patients versus healthy controls can be established (18). A PET PDE2A ligand might also be useful for assessment of agents that increase cGMP levels, such as a PDE10 inhibitor, which raised cGMP, activating PDE2A through the GAF domain (19). Thus, a PDE2A PET ligand may be useful to identify signaling interactions between pathways that alter cGMP and cAMP.

This study compared 3 kinetic models using arterial input functions. Time–activity curves were fitted well by the 2TC model

and MA1. The 2TC model and MA1 produced almost identical V_T and BP_{ND} estimates. As is often the case, the 2TC model V_T estimates were associated with large errors in some fits, whereas the MA1 V_T estimates were stable in all fits. Further, MA1 also had the favorable property that V_T estimates were little influenced by changing t^* . Thus, MA1 is the model of choice for ^{18}F -PF-05270430.

Blood volume correction was applied in this study. This correction is important when V_T is low or the parent fraction in blood is low. V_T values were low (0.7–1.4), and the parent fraction was in the medium range (40% at 120 min). The effect of blood volume correction was largest in the cerebellum, which had the lowest V_T value; lack of correction led to smaller BP_{ND} values, because of larger overestimation of cerebellar V_T . Assuming a 5% blood volume, the fraction of the cerebellum time–activity curve at 70 min accounted for by blood activity was $5\% \pm 1\%$ (mean \pm SD, $n = 11$).

The cerebellum was used as a reference region to calculate binding potentials. Western blot analysis of human brain extracts with anti-PDE2A antibodies revealed that PDE2A immunoreactivity was prominently observed in the striatum, cingulate cortex, prefrontal cortex, and hippocampus, with no detectable signal in the cerebellum (4). A blocking study in humans would be needed to validate the suitability of the cerebellum as a reference region.

The outcome measures corrected by f_B , V_T/f_B , and BP_F showed poorer reliability, because of variability of the f_B measurement, which was larger than expected. BP_{ND} and BP_P showed similar magnitudes of aTRV and TRV. However, the ICC of BP_P was poor in most regions. Therefore, BP_{ND} appears to be the best binding potential outcome measure.

V_T values were insensitive to scan duration. Over the 240-min scan, V_T values in the striatum, nucleus accumbens, and centrum semiovale showed almost no change, whereas in neocortical regions and cerebellum, V_T increased slightly (3.7%–9.1%).

TABLE 4
Binding Parameters from MA1

Region	V_T (mL/cm ³) (%COV)		V_T/f_B (mL/cm ³) (%COV)		BP_{ND} (%COV)		BP_P (mL/cm ³) (%COV)		BP_F (mL/cm ³) (%COV)	
	Test	Retest	Test	Retest	Test	Retest	Test	Retest	Test	Retest
Putamen	1.27 (11%)	1.31 (6%)	10.07 (6%)	10.14 (27%)	0.79 (20%)	0.80 (25%)	0.52 (12%)	0.54 (19%)	3.96 (14%)	4.11 (39%)
Nucleus accumbens	1.21 (15%)	1.22 (7%)	9.69 (6%)	9.49 (22%)	0.70 (16%)	0.67 (14%)	0.46 (18%)	0.45 (8%)	3.57 (16%)	3.46 (24%)
Caudate	1.03 (13%)	1.06 (6%)	8.32 (6%)	8.38 (26%)	0.45 (18%)	0.45 (30%)	0.28 (15%)	0.29 (23%)	2.20 (23%)	2.35 (46%)
Occipital cortex	1.02 (16%)	1.05 (8%)	8.29 (3%)	8.19 (22%)	0.44 (12%)	0.44 (12%)	0.27 (19%)	0.28 (6%)	2.18 (13%)	2.16 (24%)
Centrum semiovale	0.97 (18%)	1.02 (10%)	7.84 (6%)	7.79 (18%)	0.36 (21%)	0.39 (22%)	0.22 (30%)	0.25 (22%)	1.72 (26%)	1.76 (12%)
Temporal cortex	0.95 (15%)	0.99 (8%)	7.64 (3%)	7.64 (23%)	0.34 (22%)	0.36 (21%)	0.20 (23%)	0.22 (17%)	1.53 (21%)	1.61 (29%)
Frontal cortex	0.95 (14%)	0.98 (8%)	7.59 (4%)	7.59 (25%)	0.34 (22%)	0.35 (27%)	0.20 (19%)	0.21 (25%)	1.47 (19%)	1.56 (39%)
Parietal cortex	0.93 (14%)	0.95 (9%)	7.50 (4%)	7.35 (24%)	0.32 (27%)	0.30 (22%)	0.18 (28%)	0.18 (21%)	1.38 (32%)	1.32 (35%)
Cerebellum	0.71 (17%)	0.73 (12%)	5.80 (3%)	5.74 (22%)						

%COV = coefficient of variation (intersubject variability).

Values are mean of $n = 5$ subjects ($n = 4$ for V_T/f_B and BP_F), with each value measured twice in test and retest scans.

TABLE 5
Test–Retest Reproducibility of Volume of Distribution and Binding Potential

Region	MA1 (<i>t</i> * = 40 min)									SRTM		
	<i>V_T</i> (<i>n</i> = 5)			<i>BP_{ND}</i> (<i>n</i> = 5)			<i>BP_P</i> (<i>n</i> = 5)			<i>BP_{ND}</i> (<i>n</i> = 5)		
	*aTRV	*TRV	†ICC	*aTRV	*TRV	†ICC	*aTRV	*TRV	†ICC	*aTRV	*TRV	†ICC
Putamen	9%	-4% ± 11%	0.23 [-0.64, 0.87]	16%	0% ± 23%	0.58 [-0.33, 0.94]	15%	-4% ± 24%	-0.01 [-0.76, 0.80]	14%	-1% ± 22%	0.64 [-0.24, 0.95]
Nucleus accumbens	7%	-2% ± 10%	0.66 [-0.20, 0.96]	17%	4% ± 22%	0.15 [-0.69, 0.85]	14%	0% ± 23%	-0.17 [-0.83, 0.74]	14%	2% ± 18%	0.17 [-0.68, 0.86]
Caudate	7%	-3% ± 8%	0.68 [-0.17, 0.96]	18%	2% ± 21%	0.73 [-0.08, 0.97]	14%	-3% ± 19%	0.55 [-0.36, 0.94]	15%	2% ± 20%	0.83 [0.19, 0.98]
Occipital cortex	8%	-4% ± 8%	0.77 [0.03, 0.97]	12%	0% ± 16%	0.27 [-0.62, 0.88]	13%	-5% ± 18%	0.15 [-0.69, 0.85]	15%	3% ± 17%	0.36 [-0.55, 0.91]
Centrum semiovale	10%	-6% ± 11%	0.71 [-0.12, 0.96]	18%	-9% ± 19%	0.63 [-0.26, 0.95]	24%	-15% ± 22%	0.53 [-0.38, 0.94]	11%	-4% ± 14%	0.71 [-0.11, 0.96]
Temporal cortex	8%	-4% ± 9%	0.71 [-0.12, 0.96]	14%	-4% ± 24%	0.57 [-0.34, 0.94]	22%	-10% ± 28%	0.15 [-0.69, 0.85]	18%	-3% ± 26%	0.51 [-0.41, 0.93]
Frontal cortex	7%	-4% ± 7%	0.75 [-0.03, 0.97]	12%	-2% ± 16%	0.85 [0.26, 0.98]	13%	-7% ± 17%	0.69 [-0.14, 0.96]	15%	5% ± 17%	0.85 [0.26, 0.98]
Parietal cortex	5%	-2% ± 7%	0.84 [0.20, 0.98]	21%	6% ± 25%	0.65 [-0.23, 0.96]	22%	2% ± 30%	0.51 [-0.41, 0.93]	21%	9% ± 24%	0.69 [-0.16, 0.96]
Cerebellum	5%	-3% ± 6%	0.90 [0.45, 0.99]									

*TRV = (test value – retest value)/(test value + retest value) × 2, and aTRV is absolute value of TRV.

†ICC = (BSMSS – WSMSS)/(BSMSS + WSMSS) where BSMSS is mean sum of squares between subjects and WSMSS is mean sum of squares within subjects. ICC is presented with lower and upper bounds of 95% confidence interval in brackets.

Potential factors contributing to these small increases include brain uptake of radiolabeled metabolites, or spill-in from extra-brain activity (Fig. 3B). However, the minimum scan time with MA1 was 70 min in all regions under relatively strict criteria. Thus, ¹⁸F-PF-05270430 has rapid kinetics, and long acquisitions are not needed to obtain robust parameter estimates.

For *BP_{ND}*, the test–retest variability with MA1 was acceptable with 16% of aTRV and 0% of TRV on average. Although often *BP_{ND}* has better TRV than *V_T*, given the low *BP_{ND}* values (0.3–0.8), it is not surprising that the test–retest performance of *V_T* was better than *BP_{ND}*. We compared the test–retest variability data of *BP_{ND}* across several radioligands (Supplemental Table 2). The aTRV of *BP_{ND}* with ¹⁸F-PF-05270430 was poorer than many other tracers. The ICC values were low in several regions, including the putamen (0.58) and nucleus accumbens (0.15). The *V_T* and *BP_{ND}* estimates were low in all regions, indicating that ¹⁸F-PF-05270430 might only provide reliable data in the higher-binding regions, such as the putamen, caudate, and nucleus accumbens.

CONCLUSION

In this first-in-human PET study with the novel PDE2A radiotracer ¹⁸F-PF-05270430, the tracer showed rapid kinetics, providing reliable parameter estimates with a 70-min scan. MA1 is the most suitable model for describing the kinetics. Binding potential was estimated with the cerebellum as reference region, although this choice should be validated with blocking studies. ¹⁸F-PF-05270430 dosimetry showed that an effective dose was estimated as 0.023 mSv/MBq for a 70-kg male. On the basis of the results of this study, ¹⁸F-PF-05270430 is a suitable PDE2A PET ligand and can be reliably used in future clinical studies to assess enzyme occupancy levels of PDE2A inhibitors.

DISCLOSURE

The costs of publication of this article were defrayed in part by the payment of page charges. Therefore, and solely to indicate this fact, this article is hereby marked “advertisement” in accordance with 18 USC section 1734. This study was sponsored by Pfizer, Inc. This publication was also made possible by CTSA grant UL1 RR024139 jointly from the National Center for Research Resources (NCRR) and the National Center for Advancing Translational Sciences (NCATS), components of the National Institutes of Health (NIH). Its contents are solely the responsibility of the authors and do not necessarily represent the official view of NIH. No other potential conflict of interest relevant to this article was reported.

ACKNOWLEDGMENTS

We appreciate the excellent technical assistance of the staff at the Yale University PET Center and the Pfizer CRU and the support of the Yale–Pfizer Bioimaging Alliance.

REFERENCES

- Conti M, Beavo J. Biochemistry and physiology of cyclic nucleotide phosphodiesterases: essential components in cyclic nucleotide signaling. *Annu Rev Biochem.* 2007;76:481–511.
- Pandit J, Forman MD, Fennell KF, Dillman KS, Menniti FS. Mechanism for the allosteric regulation of phosphodiesterase 2A deduced from the x-ray structure of a near full-length construct. *Proc Natl Acad Sci USA.* 2009;106:18225–18230.
- Stephenson DT, Coskran TM, Kelly MP, et al. The distribution of phosphodiesterase 2A in the rat brain. *Neuroscience.* 2012;226:145–155.
- Stephenson DT, Coskran TM, Wilhelms MB, et al. Immunohistochemical localization of phosphodiesterase 2A in multiple mammalian species. *J Histochem Cytochem.* 2009;57:933–949.
- Zhang L, Villalobos A, Beck EM, et al. Design and selection parameters to accelerate the discovery of novel central nervous system positron

- emission tomography (PET) ligands and their application in the development of a novel phosphodiesterase 2A PET ligand. *J Med Chem.* 2013;56:4568–4579.
6. Chen L, Nabulsi N, Naganawa M, et al. Preclinical evaluation of ¹⁸F-PF-05270430, a novel PET radioligand for the phosphodiesterase 2A enzyme. *J Nucl Med.* May 19, 2016 [Epub ahead of print].
 7. Cristy M, Eckerman KF. *Specific Absorbed Fractions of Energy at Various Ages from Internal Photon Sources. I. Methods.* Oak Ridge, TN: Oak Ridge National Laboratory; 1987. ORNL/TM-8381/V8381.
 8. Stabin MG, Sparks RB, Crowe E. OLINDA/EXM: the second-generation personal computer software for internal dose assessment in nuclear medicine. *J Nucl Med.* 2005;46:1023–1027.
 9. Hilton J, Yokoi F, Dannals RF, Ravert HT, Szabo Z, Wong DF. Column-switching HPLC for the analysis of plasma in PET imaging studies. *Nucl Med Biol.* 2000;27:627–630.
 10. Tzourio-Mazoyer N, Landeau B, Papathanassiou D, et al. Automated anatomical labeling of activations in SPM using a macroscopic anatomical parcellation of the MNI MRI single-subject brain. *Neuroimage.* 2002;15:273–289.
 11. Holmes CJ, Hoge R, Collins L, Woods R, Toga AW, Evans AC. Enhancement of MR images using registration for signal averaging. *J Comput Assist Tomogr.* 1998;22:324–333.
 12. Papademetris X, Jackowski M, Rajeevan N, Constable RT, Staib LH. Bioimage suite: an integrated medical image analysis suite. *Insight J.* 2006;2006:209.
 13. Gallezot JD, Nabulsi N, Holden D, et al. Development of a lysophosphatidic acid receptor 1 (LPA₁) radioligand for lung imaging with PET [abstract]. *J Nucl Med.* 2014;55(suppl 1):96.
 14. Frankle WG, Huang Y, Hwang DR, et al. Comparative evaluation of serotonin transporter radioligands ¹¹C-DASB and ¹¹C-McN 5652 in healthy humans. *J Nucl Med.* 2004;45:682–694.
 15. Gallezot JD, Zheng MQ, Lim K, et al. Parametric imaging and test-retest variability of ¹¹C-(+)-PHNO binding to D2/D3 dopamine receptors in humans on the high-resolution research tomograph pet scanner. *J Nucl Med.* 2014;55:960–966.
 16. Gomez L, Breitenbucher JG. PDE2 inhibition: potential for the treatment of cognitive disorders. *Bioorg Med Chem Lett.* 2013;23:6522–6527.
 17. Morgan P, Van Der Graaf PH, Arrowsmith J, et al. Can the flow of medicines be improved? Fundamental pharmacokinetic and pharmacological principles toward improving phase II survival. *Drug Discov Today.* 2012;17:419–424.
 18. Maurice DH, Ke H, Ahmad F, Wang Y, Chung J, Manganiello VC. Advances in targeting cyclic nucleotide phosphodiesterases. *Nat Rev Drug Discov.* 2014;13:290–314.
 19. Rombouts FJ, Tresadern G, Buijnsters P, et al. Pyrido[4,3-e][1,2,4]triazolo[4,3-a]pyrazines as selective, brain penetrant phosphodiesterase 2 (PDE2) inhibitors. *ACS Med Chem Lett.* 2015;6:282–286.



The Journal of
NUCLEAR MEDICINE

First-in-Human Assessment of the Novel PDE2A PET Radiotracer ^{18}F -PF-05270430

Mika Naganawa, Rikki N. Waterhouse, Nabeel Nabulsi, Shu-Fei Lin, David Labaree, Jim Ropchan, Sanela Tarabar, Nicholas DeMartinis, Adam Ogden, Anindita Banerjee, Yiyun Huang and Richard E. Carson

J Nucl Med. 2016;57:1388-1395.
Published online: April 21, 2016.
Doi: 10.2967/jnumed.115.166850

This article and updated information are available at:
<http://jnm.snmjournals.org/content/57/9/1388>

Information about reproducing figures, tables, or other portions of this article can be found online at:
<http://jnm.snmjournals.org/site/misc/permission.xhtml>

Information about subscriptions to JNM can be found at:
<http://jnm.snmjournals.org/site/subscriptions/online.xhtml>

The Journal of Nuclear Medicine is published monthly.
SNMMI | Society of Nuclear Medicine and Molecular Imaging
1850 Samuel Morse Drive, Reston, VA 20190.
(Print ISSN: 0161-5505, Online ISSN: 2159-662X)

© Copyright 2016 SNMMI; all rights reserved.